

1 **4D imaging of fracturing in organic-rich shales during heating**

2

3 *Maya Kobchenko¹, Hamed Panahi^{1,2}, François Renard^{1,3}, Dag K. Dysthe¹, Anders Malthe-*

4 *Sørenssen¹, Adriano Mazzini¹, Julien Scheibert^{1,4}, Bjørn Jamtveit¹ and Paul Meakin^{1,5,6}*

5

6 ¹ Physics of Geological Processes, University of Oslo, Norway

7 ² Statoil ASA, Oslo, Norway

8 ³ Institut des Sciences de la Terre, Université Joseph Fourier and CNRS, Grenoble, France

9 ⁴ Laboratoire de Tribologie et Dynamique des Systèmes, CNRS, Ecole Centrale de Lyon, Ecully CEDEX,
10 France.

11 ⁵ Idaho National Laboratory, Idaho Falls, USA

12 ⁶ Institute for Energy Technology, Kjeller, Norway

13

14 **Abstract**

15 To better understand the mechanisms of fracture pattern development and fluid escape in
16 low permeability rocks, we performed time-resolved *in situ* X-ray tomography imaging to
17 investigate the processes that occur during the slow heating (from 60° to 400°C) of organic-rich
18 Green River shale. At about 350°C cracks nucleated in the sample, and as the temperature
19 continued to increase, these cracks propagated parallel to shale bedding and coalesced, thus
20 cutting across the sample. Thermogravimetry and gas chromatography revealed that the
21 fracturing occurring at ~350°C was associated with significant mass loss and release of light
22 hydrocarbons generated by the decomposition of immature organic matter. Kerogen
23 decomposition is thought to cause an internal pressure build up sufficient to form cracks in the
24 shale, thus providing pathways for the outgoing hydrocarbons. We show that a 2D numerical
25 model based on this idea qualitatively reproduces the experimentally observed dynamics of crack
26 nucleation, growth and coalescence, as well as the irregular outlines of the cracks. Our results
27 provide a new description of fracture pattern formation in low permeability shales.

28

29 **Key words:** primary migration, shale, X-ray computed micro-tomography, kerogen,
30 hydrocarbon, reaction fracturing

31

32 **1. Introduction**

33 A wide variety of geological phenomena involve the generation and migration of fluids in
34 low permeability rocks. For example, dehydration of sediments in subduction zones generates
35 large fluxes of water that rise along low-permeability subduction interfaces, and provide a
36 mechanism for creep and/or slow earthquakes [Obara, 2002]. Similarly, the illitization of clays
37 at depth and the production of methane in organic-rich shales were suggested to contribute to the
38 development of overpressure and the formation of piercement structures, which are manifest on
39 the surface as mud volcanoes [Mazzini *et al.*, 2009]. Also, the emplacement of magmatic bodies
40 into sedimentary basins induces rapid decomposition of organic matter, and the resulting gases
41 migrate through low permeability rocks in quantities that may significantly alter the climate
42 [Svensen *et al.*, 2004]. In all these geological systems, the migration of a fluid through low
43 permeability rocks is coupled with deformation. This type of coupling between fluid flow and
44 deformation is also important in the primary migration of hydrocarbons.

45 Primary migration is the transport of hydrocarbon fluids from extremely low permeability
46 source rocks, in which they are generated, to more permeable rocks through which they migrate
47 to a trap (reservoir) or to the surface. This natural process is of both economic and fundamental
48 interest. As the organic-rich fine grained sediment from which the source rock is formed is
49 buried, the organic material is transformed into complex high molecular weight/cross-linked
50 organic oil and gas precursors (kerogen). As the burial depth increases, the temperature and
51 pressure rise, and kerogen decomposes into low molecular weight hydrocarbon fluids (gas and
52 oil), which have much lower viscosities than the kerogen. The generated hydrocarbon fluids
53 escape from the shale into secondary migration pathways, by processes that remain enigmatic, in
54 spite of decades of investigation [Bjørlykke, 2010].

55 Fracturing is commonly cited as a likely mechanism to increase the permeability of
56 source rocks and provide pathways for the generated hydrocarbons [*Berg and Gangi, 1999; Lash*
57 *and Engelder, 2005*]. During kerogen decomposition, generation of less dense fluids leads to
58 pore-pressure build-up, which may cause fracturing of the host rock. The presence of
59 microcracks is commonly observed in thin sections of recovered source rock samples [*Capuano,*
60 *1993; Vernik, 1993; Marquez and Mountjoy, 1996; Lash and Engelder, 2005*], suggesting that
61 microcracks may be involved in fluid migration.

62 Under natural conditions, this fracture process takes place at depths of several kilometers
63 over millions of years, making its monitoring impossible. Therefore, it is very important to
64 construct adequate models of primary migration. Several theoretical and numerical studies of
65 fracture formation in organic-rich shales have been described in the scientific literature [*Ozkaya,*
66 *1988; Jin et al., 2010*]. *Jin et al.* [2010] introduced a fracture mechanics model of subcritical
67 crack propagation and coalescence, based on the assumption of linear elastic behavior of the
68 rock. Although the model provides an estimate of the fracture propagation time, the 3D geometry
69 and mechanism of fracture formation in heterogeneous shale remain unclear.

70 To better understand the complex phenomenon of hydrocarbon expulsion from very low
71 permeability source rock, we employed a new experimental approach – real-time 3D X-ray
72 tomography – during gradual heating of a shale sample coupled with thermogravimetry and
73 petrography analyses before and after heating. This study included only unconfined samples, but
74 it is an important step towards the goal of unraveling the numerous and complex mechanisms
75 controlling primary migration.

76 **2. Characterization of Green River Shale samples**

77 The samples were obtained from an outcrop of the organic-rich R-8 unit of the Green
78 River Shale Formation (Piceance Basin, northwestern Colorado, USA). The formation consists
79 of Eocene lacustrine marl/silt sediments [Ruble *et al.*, 2001] with well-developed lamination and
80 anisotropic mechanical properties [Vernik and Landis, 1996]. It contains organic matter (total
81 organic content = 9.92 wt% in analyzed samples) present in the form of patches of kerogen,
82 preferentially distributed parallel to the bedding (Figure 1A, B). This part of the formation has
83 never been buried deeply enough to reach temperatures sufficient to cause significant thermal
84 maturation.

85 Cylindrical core samples (5mm height, 5mm in diameter) cut perpendicular to the
86 bedding were prepared for X-ray tomography. Thin sections were taken before and after heating.
87 Optical microscope images (Figure 1A, B) highlight the micro-fabric of the uncooked shale
88 consisting of alternating lamellae of: coarser and lighter colored carbonate cemented layers rich
89 in siliciclastic grains (e.g. quartz) and pyrite framboids; and darker and finer grained clay-rich
90 layers, containing greater amount of discontinuous organic matter lenses.

91 **3. 4D imaging and data processing**

92 Time-lapse X-ray tomography 3D imaging of the shale samples was carried out using
93 beamline ID19 at the European Synchrotron Radiation Facility in Grenoble, France. This non-
94 invasive imaging technique measures the absorption of X-rays, to produce a 3D attenuation map.

95 The prepared shale cylinder was placed in a home-built furnace in contact with air, with
96 no confining pressure, and it was gradually heated *in-situ* from 60°C to 400°C at approximately
97 1°C/min. 68 3D scans of this sample were taken, of which 28 were acquired during the heating
98 phase and the rest at 400°C. For all scans, 1500 radiographs were acquired while the sample was
99 rotated over 180°. The beam energy of 20 keV allowed images to be captured with a spatial

100 resolution of 5 μm ($5 \times 5 \times 5 \mu\text{m}^3$ voxels) and a time resolution of 11-14 minutes per 3D scan. 3D
101 raw-tomograms representing the microporous structure of the sample at different stages of
102 heating were constructed from the X-ray data. The final volumes contained 830^3 voxels coded in
103 8-bit gray levels.

104 The 3D images were processed in two ways. First, the strain field was measured in a
105 typical 2D vertical slice of the volume, using digital image correlation [*Rechenmacher and*
106 *Finno, (2004); Hild and Roux, 2006; Viggiani, (2009); Bornert et al, 2010*]. Second, in order to
107 determine crack geometries and track crack propagation, the shape, volume and morphology of
108 the cracks were analyzed in 3D using the AvizoFire© software package. Quantitative analysis of
109 the crack formation required isolation of the cracks from the rock matrix. Due to the small crack
110 opening (4-5 voxels), the following procedure was applied: firstly a binary mask was used to
111 delete the background; then an edge-preserving smoothing filter based on Gaussian smoothing
112 combined with a non-linear diffusion algorithm was applied; then a “watershed” procedure
113 enabled individual cracks to be isolated [*Sonka et al, 1999*]. The final result of this segmentation
114 procedure was a series of cracks consisting of connected voxels, marked by different
115 labels/colors (Figure 2A).

116 **4. Observation of deformation and crack formation**

117 Correlation analysis and 3D image analysis were performed to determine the deformation
118 of the sample before fracturing and the geometries of the developing cracks. The spatial
119 fluctuations of the attenuation maps (see Figure 2B) served as markers when the digital
120 correlation technique was used to compare successive images. To calculate the correlation matrix
121 we used a correlation box of size 25 by 25 pixels ($125 \text{ by } 125 \mu\text{m}^2$), which enabled us to measure
122 the spatial distribution of micro-displacements.

123 Between room temperature and 300°C, the shale dilated anisotropically in the vertical
124 (perpendicular to the shale bedding) and horizontal (parallel to the shale bedding) directions, and
125 the strain curves showed a quasi-linear increase with temperature, as expected for linear thermal
126 expansion (Figure 3A). The coefficient for thermal expansion was determined to be $5.5 \cdot 10^{-5}/^{\circ}\text{C}$
127 in the vertical direction and $2.5 \cdot 10^{-5}/^{\circ}\text{C}$ in the horizontal direction, which clearly indicates the
128 anisotropy of the shale, in agreement with other studies on the same shale [Grebowicz, 2008]. At
129 300°C, the vertical expansion started to deviate from linearity, which is likely related to the onset
130 of organic degassing before crack formation. At a temperature of about 350°C the sample
131 undergoes rapid localized deformation owing to fluid generation and the onset of fracturing. The
132 sample breaks, black structures corresponding to the newly formed cracks appear in the images
133 (see Figure 2B), which have no equivalent in the preceding ones, thus ruining the correlation
134 technique. Moreover, after the sample fractures, global movement of the sample occurs
135 (translation and rotation), with displacements from one data set to the next of amplitude greater
136 than 12 pixels, which was estimated to be the maximum displacement that can be accurately
137 measured using the correlation technique. Even though the correlation results during and after
138 fracturing are not trustworthy, this technique accurately determines the sample deformation
139 before fracturing occurs.

140 With 3D tomography, we imaged 3 stages of fractures propagation. The first
141 microfracture pattern was detected at a temperature of about 350°C. Figure 2A shows a 3D
142 rendering of the most opened fractures at $T=391^{\circ}\text{C}$ (third time step) and Figures 2B and 2C show
143 a vertical slice through the tomography image. The general direction of crack propagation
144 followed the shale bedding, and no perpendicular fractures were observed (Figure 2B). Pyrite

145 grains, observable as bright spots in the tomography images (Figure 2C), affected crack growth
146 by pinning the crack front, and controlling the out-of-plane fluctuations of the crack path.

147 The fractures can be described in terms of two rough, essentially parallel surfaces that
148 enclose the fracture aperture. Both surfaces can be described by height functions, $h_1(x,y)$ and
149 $h_2(x,y)$, where (x,y) is the position in the common plane. Figure 4A shows the topography of
150 fracture surface $h_1(x,y)$, where the fluctuation of surface function $h_1(x,y)$ around the flat plane
151 (x,y) is indicated by the color code. Cracks have essentially constant aperture widths - the
152 thickness function $h_2(x,y) - h_1(x,y)$ (4-5 pixels, i.e. 20-25 micrometers, see Figure 4B), and rough
153 irregular outlines. The amplitude of the topography variation is around 10-15 pixels (i.e. 50-75
154 micrometers), as seen in the Figure 4A. The mid-plane ($H(x,y) = [h_1(x,y) + h_2(x,y)]/2$) is also
155 rough, and it fluctuates about a flat plane – the “plane of the fracture”. The projections of $h_1(x,y)$,
156 $h_2(x,y)$ and $([h_1(x,y) + h_2(x,y)]/2)$ into this plane, in a direction perpendicular to the plane, have a
157 common shape, which consists of a continuous region with rough edges. When one fracture
158 coalesces with another, a new fracture is formed, and it can be described in terms of the rough
159 surfaces $H^{new}(x,y)$, $h_1^{new}(x,y)$ and $h_2^{new}(x,y)$. The projections of these rough surfaces are also a
160 common shape, which consists of a continuous region with rough edges. The planes of the
161 coalesced fracture and the two fractures that coalesced to form it are more-or-less parallel, and
162 also quasi-parallel to the shale lamination. Viewed from “above”, in the direction perpendicular
163 to the plane of the fractures and the lamination, the fractures are continuous, and they grow and
164 coalesce in three successive stages (Figure 5A). As the temperature rose, cracks nucleated (1),
165 grew and coalesced in a quasi-static manner (2) until they spanned the sample (3). The growth of
166 the surface area of the biggest fracture with increasing temperature is shown in Figure 3D.

167 **5. Organic decomposition induces fracturing in the shale**

168 Thin sections were studied in order to compare petrographic characteristics of the shale
169 before and after heating. Before heating, organic precursors, which were preferentially oriented
170 parallel to the shale bedding, could be distinguished throughout the sample (see Figure 1A, B).
171 After heating, an abundance of cracks, partially filled with residual organic material, was
172 distributed parallel to the bedding (Figure 1C, D). Petrographic observations revealed that cracks
173 propagated mainly in the finer grained layers where the highest concentrations of organic matter
174 lenses were observed (Figure 1A, C). The coarser grained layers, where quartz grains and pyrite
175 framboids were present in higher concentration, also displayed better cementation with larger
176 calcite crystals. The preferential location of fracture propagation is ascribed to two main factors:

- 177 a) Higher amounts of organic matter (kerogen lenses), which decomposes leading to fluid
178 formation, internal pressure build up and eventually fracture initiation and propagation.
- 179 b) Finer grained intervals are less cemented than the coarser grained ones and they fracture
180 more easily.

181 The link between hydrocarbon generation and fracturing was tested using thermogravimetry and
182 gas chromatography. Aerobic and anaerobic (nitrogen) thermo-gravimetry analyses on 500 mg
183 samples were performed to investigate the presence of organic and inorganic carbon (carbonates)
184 using a ATG/SDTA 851 Mettler Toledo apparatus. We monitored mass loss of the sample during
185 heating at 10°C/min in air or nitrogen between 20°C and 1000°C. The loss of mass during
186 heating occurred in distinct stages (Figure 3B), and the temperature range of each stage indicates
187 the nature of the component that evaporates. We also used gas chromatography (GC 5890-MS
188 5973 Agilent) to analyze the gas that escaped (water, CO₂, and organic volatiles) during heating
189 at a rate of 5°C/min in air. The first step of mass loss (Figure 3B) in the temperature range 300 -
190 450°C corresponds to the release of various organic molecules (alkanes, alkenes, toluene,

191 xylenes), water and CO₂ (first peak on CO₂ emission plot) and indicates decomposition of
192 organic matter. The second step of mass loss around 600 - 800°C indicates decomposition of
193 carbonates. A similar behavior was observed when nitrogen was used instead of air with two
194 peaks of CO₂ release located at the same temperatures.

195 Figure 6 shows the correlations between strain evolution, mass loss, CO₂ emission and
196 fracture surface area growth. Comparing the temperatures of degassing, mass loss and
197 hydrocarbon release with the temperature of fracturing onset, we conclude that fracturing was
198 induced by overpressure in the sample caused by organic matter decomposition.

199 **6. Discrete model of crack propagation**

200 Based on the experimentally observed fracturing behavior (Figure 5A), a two
201 dimensional (2D) model of in-plane crack nucleation and growth due to internal pressure
202 increase was developed (Figure 7). The choice of a 2D model is based on the observation of
203 planar mode I cracks that follow the layering of the shale and the focus on in-plane dynamics
204 rather than the placement of cracks and relation between cracks normal to their plane. To
205 reproduce key characteristics of the crack growth process including the merging of small cracks
206 and the very irregular crack shapes, we used a statistical fracture model [Alava *et al.*, 2006]. The
207 main parameter needed is the variability of local strength, and the model neglects long range
208 effects of the stress field. The model includes neither the kinetics of kerogen decomposition nor
209 the elastic properties of the source rock, and therefore it cannot quantitatively predict threshold
210 temperatures and pressures, or rates of primary migration. The objective of the model is to find
211 the minimum number of features that explain the observed behavior. The macroscopic fracture
212 threshold and kerogen transformation kinetics are important to predict at what temperature and
213 rate these phenomena occur, but they do not help us understand how the fracture evolves. The

214 percolation like evolution of the fracture, as opposed to the nucleation of a single fracture that
215 propagates rapidly through the shale, which would be predicted by a macroscopic elastic model
216 with a distributed pressure build-up, shows that the material disorder may cause the slow
217 formation of percolating fluid pathways for expulsion of hydrocarbon fluids at pressures much
218 smaller than those needed to completely fracture the shale. The model focuses on a layer of shale
219 that fractures more rapidly than nearby layers because it has a higher kerogen content. The layer
220 is modeled by a regular square lattice in which every site represents a small organic-rich shale
221 element. Each site is characterized by a randomly assigned breaking threshold $\sigma_{c,i}$. The pressure
222 in the lattice rises incrementally during each time step and, when it exceeds the breaking
223 threshold ($p_i > \sigma_{c,i}$), the site fractures to represent either nucleation of a new crack or growth of a
224 pre-existing crack. This relaxes the stress, which is distributed equally to the nearest non-broken
225 neighbors (long-range elastic interactions are neglected), bringing them closer to failure. The
226 distribution of stress was implemented by reducing the breaking threshold, $\sigma_{c,i} \rightarrow \sigma_{c,i} - d\sigma$, for
227 all nearest non-broken neighbors. Dimensionless units were used for the pressure and breaking
228 thresholds. Each crack is represented by a cluster of broken sites. As soon as sites belonging to
229 different clusters become adjacent, both clusters are merged to form a single crack, and all the
230 merged sites are given the same label/color.

231 Figure 5B shows three successive snapshots during a simulation. In the early stage, the
232 system contains many small independent cracks. Each crack has a rough front, and over time,
233 individual cracks grow slowly and merge until the whole plane is covered. Figure 3C displays
234 the increase of the area of the largest final simulated crack. Crack growth occurs in three stages:
235 (1) the microcracks are all separated and their surface areas grow gradually; (2) the cracks start
236 to coalesce, the rate at which the fractured area increases accelerates, and growth in the total

237 fracture area is dominated by distinct jumps and (3) ultimately the system is dominated by one
238 large fracture, with an area that grows by intermittent increases (see also the corresponding
239 snapshots 1-3 in Figure 5B). The qualitative trend of the fracture area growth in the simulation
240 (Figure 3C) is similar to that observed in the experiment (Figure 3D).

241 The model is similar to the fiber bundle model with local load sharing, which has been
242 intensively studied model for material failure [Pradhan, 2010]. We suggest that it can be applied
243 to other geological systems in which chemical reactions induce volume increase and stress build-
244 up in rocks. These systems are widespread and include, apart from primary migration of
245 hydrocarbons, weathering of rocks near the surface [Røyne *et al.*, 2008] and dehydration of
246 serpentines in subduction zones [Jung *et al.*, 2004].

247

248 **7. Discussion and Conclusion**

249 Time-resolved high-resolution synchrotron X-rays tomography was performed during
250 gradual heating (from 60 to 400°C) of organic-rich immature shales. At 350 °C the nucleation of
251 many small cracks was detected. With further temperature increase these microcracks propagated
252 parallel to the shale bedding, coalesced and ultimately spanned the whole sample.

253 The central point of our work is the observed correlation between hydrocarbon expulsion
254 and fracturing within the sample. To do this, we combined thermogravimetry, gas
255 chromatography, strain analysis and 3D observation of fracture formation and analyze the data in
256 3 steps:

- 257 - Analyzing tomograms, we found that that fracturing begins at a temperature of about
258 350°C.

259 - Using thermogravimetry, we determined that the sample started to loose mass in the same
260 temperature range (about 350°C). This alone does not provide us with the composition of
261 the lost material.

262 - Using gas chromatography, we determine that the gases expelled at temperatures near
263 350°C were mainly oxidized hydrocarbons, and we conclude that they originate from
264 kerogen decomposition.

265 In the literature, some shale rocks are reported to contain horizontal in the direction of
266 shale bedding (mode I) fractures as well as vertical (perpendicular to the shale bedding)
267 fractures. The presence of vertical fractures indicates that the maximum stress is vertical [*Olson,*
268 *1980; Smith, 1984*]. However at shallow depths, where the magnitudes of both the vertical and
269 horizontal stresses are similar, horizontal hydro-fractures of significant lateral extent can be
270 created due to anisotropy of shales [*Thomas, 1972; Jensen, 1979*]. Horizontal fractures are also
271 observed to develop in clay-rich shales in response to high overpressures during maturation
272 [*Littke, 1988*], even in regions where the vertical stress is larger than the horizontal stress. The
273 reason for this is thought to be the strong lamination of these shales [*Lash and Engelder, 2005;*
274 *Vernik, 1993*]. Theoretical studies [*Ozkaya, 1988*] also showed that vertical cracks are unlikely to
275 form by oil generation and the excess of oil pressure is sufficient to cause lateral fracturing if the
276 aspect ratio of kerogen patches is sufficiently large.

277 In nature petroleum generation takes place in the 80-150°C temperature range, and this
278 occurs typically over time periods of 1-100 million years (up to 500 million in some geological
279 situations). The heating rate for a basin like the North Sea is 1-2°C/million years, but during
280 rapid sedimentation and subsidence the heating rate is as high as 10°C/million years [*Bjorlykke,*

281 2010]. In our experiments, conducted in a much shorter time, fracturing was observed to occur in
282 the temperature range of 300-400°C.

283 The decomposition of kerogen involves a very large number of coupled chemical
284 reactions, and a temperature dependent rate constant is associated with each reaction. In general,
285 the rates of these reactions can be represented approximately by the Arrhenius function $K_i =$
286 $A_i T^n \exp(-E_i^a/RT)$, where K_i is the rate constant for the i^{th} reaction, A_i is its frequency factor, E_i^a is
287 its activation energy, R is the gas constant and T is the absolute temperature. In most cases, n is
288 small, the temperature dependence is dominated by the exponential term and the Arrhenius
289 equation is often expressed in the form $A_i' \exp(-E_i^a/RT)$. The overall rate of the organic maturation
290 process, K , can also be represented by a similar Arrhenius function $K = A \exp(-E^a/RT)$, although
291 the nature of the decomposition products is also somewhat temperature dependent. If the
292 activation energy, E^a , is large enough, the maturation rate increases rapidly with increasing
293 temperature, and this explains why a higher temperature can be used to accelerate the maturation
294 process and achieve a maturation time that is short enough to conduct laboratory experiments.

295 Under natural conditions cracks form during maturation at lower temperature, and
296 because of the low rate of pressure buildup crack growth is probably a slow subcritical fracturing
297 process. Based on theoretical calculations by [Ozkaya, 1988], we can estimate the conditions for
298 the initiation of lateral cracking. [Ozkaya, 1988] considered a linearly elastic and isotropic source
299 rock containing isolated kerogen flakes enclosed in an impermeable shale matrix, and showed
300 that the aspect ratio of the kerogen particles may influence the initiation of horizontal
301 microcracks in the source rock beds under maximum vertical principal stress. Initiation of
302 microcracks as a function of kerogen flakes shape occurs when:

303
$$\Delta P \left(\frac{2w}{h} - 1 \right) > S_v (2 - k) + C, \quad [1]$$

304 where S_v is the principal vertical stress, k is the lateral to vertical stress ratio, C is the strength of
305 the rock, ΔP is the excess oil pressure induced during kerogen decomposition, w is the length of
306 kerogen particle, and h is the thickness of kerogen particles. For example, for the kerogen patch
307 shown on the Figure 1C, the aspect ratio is $w/h=50\mu\text{m}/3\mu\text{m}\approx 16$. For $k=0.75$, $\Delta P=5\text{Mpa}$,
308 $C=10\text{MPa}$ [Ozkaya, 1988], equation [1] indicates that lateral fracturing may occur if the vertical
309 stress S_v is lower than 116 MPa, which corresponds to a depth h smaller than 4000 m.

310 One limitation of this calculation is the assumption that the kerogen patches are
311 surrounded by impermeable rock. In reality, shales have very small permeabilities and the
312 transformation reaction is slow. The generated fluids may migrate through the rock matrix
313 without producing pressure gradients that are large enough to cause fracturing. However magma
314 emplacement in sedimentary basins may result in much higher maturation rates and the rapid
315 production of hydrocarbon fluids may cause rapid internal pressure build up and fracture
316 generation.

317 To summarize our observations, correlation analysis monitoring of the deformation of the
318 sample indicated abrupt swelling perpendicular to the bedding just before the cracks formation.
319 Petrography observations showed that the main cracks initiate in the finer grained clay-rich
320 layers where a higher amount of organic matter is present. Thermogravimetry and gas
321 chromatography analyses showed that the sample began to lose significant mass and release
322 water, CO_2 and hydrocarbon gasses at about 350°C . These observations support a scenario in
323 which the kerogen, present in thin lenses, starts to decompose around 350°C , causing volume
324 increase and internal pressure build up leading to fracturing. The fracturing mechanism observed
325 experimentally, including crack formation and crack geometry, was successfully reproduced by a
326 2D fiber-bundle lattice simulation. The success of the statistical fracture model indicates that

327 material disorder and local elastic interactions play a key role in the development of the observed
328 percolation like fracture. The implication is that percolating low permeability fluid pathways are
329 formed in the shale long before macroscopic fracturing occurs.

330 In the present study we do not characterize fracturing of source rocks under natural
331 conditions. In particular, no confinement was applied to the sample. We therefore suggest that
332 the results of our experiments can be directly relevant to better understand induced fracturing of
333 shales located at shallow depth or outcrops, where the confinement pressure is low. More
334 generally, the methods developed here will be relevant for future studies under more realistic
335 conditions.

336

337 **Acknowledgments:** We acknowledge support by the Petromaks program of the
338 Norwegian Research Council. We thank Elodie Boller at ESRF for her help during the
339 tomography scans and Rodica Chiriac for her help with the thermogravimetry analyses.

340

341 **References**

- 342 Alava, M. J., Nukalaz P. K. V. V., and S. Zapperi (2006), Statistical models of fracture,
343 *Advances in Physics*, 55, 349-476.
- 344 Berg, R.R., and A.F. Gangi (1999), Primary migration by oil-generation microfracturing in low-
345 permeability source rocks: application to the Austin Chalk, Texas, *AAPG Bull.*, 83, 727-756.
- 346 Bjørlykke, K. (2010), Petroleum Geoscience: From Sedimentary Environments to Rock Physics,
347 *Springer, Berlin, Germany*.
- 348 Bornert, M., Vales, F., Gharbi, H., and D.N. Minh (2010), Multiscale full-field strain
349 measurements for micromechanical investigations of the hydromechanical behaviour of clayey
350 rocks, *J. Geophys. Res.*, 46, 33-46.
- 351 Capuano, R.M. (1993), Evidence of fluid flow in microcracks in geopressed shales, *AAPG*
352 *Bull.*, 77, 1303-1314.
- 353 Grebowicz, J. (2008), Thermal properties of Green River oil shales, Joint Meeting of The
354 Geological Society of America, Soil Science Society of America, American Society of
355 Agronomy, Crop Science Society of America, Gulf Coast Association of Geological Societies
356 with the Gulf Coast Section of SEPM, 2-10 October 2008, Houston TX, paper 346-1.
- 357 Hild, F., and S. Roux (2006), Digital Image Correlation: from Displacement Measurement to
358 Identification of Elastic Properties – a Review, *Strain*, 42, 69-80.
- 359 Jensen, H.B. Oil shale in situ research and development // Talley Energy systems final report, US
360 Department of Energy DOE/ LC/ 01791-T1, 1979.
- 361 Jin, Z.-H., S. E. Johnson, and Z. Q. Fan (2010), Subcritical propagation and coalescence of oil-
362 filled cracks: Getting the oil out of low-permeability source rocks, *Geophys. Res. Lett.*, 37,
363 L01305.

364 Jung, H. (2004), Intermediate-depth earthquake faulting by dehydration embrittlement with
365 negative volume change, *Nature*, 428, 6982, 545-549.

366 Lash, G.G., and T. Engelder (1992), An analysis of horizontal microcracking during catagenesis:
367 Example from Catskill delta complex, *AAPG Bull.*, 89, 1433-1449.

368 Lash, G.G., and T. Engelder (2005), An analysis of horizontal microcracking during catagenesis:
369 Example from Catskill delta complex, *AAPG Bull.*, 89, 1433-1449.

370 Littke, R., Baker, D.R., and D. Leythaeuser (1988), Microscopic and sedimentologic evidence
371 for the generation and migration of hydrocarbons in Toarcian source rocks of different
372 maturities, *Org. Geochemistry*, 13, 549-559.

373 Marquez, X.M., and E.W. Mountjoy (1996), Microcracks due to overpressure caused by thermal
374 cracking in well-sealed Upper Devonian reservoirs, deep Alberta basin, *AAPG Bull.*, 80, 570-
375 588.

376 Mazzini, A. (2009), Mud volcanism: Processes and implications, *Marine and Petroleum*
377 *Geology*, 26(9): 1677-1680.

378 Obara, K. (2002), Nonvolcanic deep tremor associated with subduction in southwest Japan,
379 *Science*, 296, 1679-1681.

380 Olson, W.A. (1980), Stress relaxation in oil shale. In: Proc. 21st Symposium on Rock Mechanics,
381 517-520.

382 Ozkaya, I. (1988), A simple analysis of oil-induced fracturing in sedimentary rocks, *Marine and*
383 *Petroleum Geology*, 5, 293-297.

384 Pradhan, S., Hansen, A. and B. K. Chakrabarti (2010), Failure processes in elastic fiber bundles,
385 *Rev. Mod. Phys.*, 5, 499-555.

386 Rechenmacher, A.L., and R.J. Finno (2004), Digital image correlation to evaluate shear banding
387 in dilative sands, *Geotechn. Testing J.*, 27, 13-22.

388 Røyne, A., Jamtveit, B., Mathiesen, J., and A. Malthe-Sorrensen (2008), Controls of rock
389 weathering rates by reaction-induced hierarchical fracturing, *Earth Planet. Sci. Lett.*, 275, 364-
390 369.

391 Ruble, T. E., M.D. Lewan, and R.P. Philp (2001), New insights on the Green River petroleum
392 system in the Uinta basin from hydrous pyrolysis experiments, *AAPG Bull.*, 85, 1333 -1371.

393 Sandvik, E.I. and J.N. Mercer (1990), Primary migration by bulk hydrocarbon flow. *Adv. In Org.*
394 *Geochemistry*, 16, 83-89.

395 Smith, J.W., and Chong, K.P. (1984) Introduction to mechanics of oil shale. In: Chong, K.P.,
396 Smith, J.W. (Eds): *Mechanics of Oil Shale*. Elsevier, 198, 1-41.

397 Sonka, M., Hlavac, V., and R. Boyle (1999), *Image processing, analysis and machine vision*,
398 *PWS Publishing, Pacific Grove, CA, USA*.

399 Svensen, H., Planke, S., Malthe-Sorensen, A., Jamtveit, B., Myklebust, R., Eidem, T.R., and
400 S.S. Rey (2004), Release of methane from a volcanic basin as a mechanism for initial Eocene
401 global warming, *Nature*, 429, 6991, 542-545.

402 Thomas, H.E. (1972), Hydraulic fracturing of Wyoming Green River oil shale: field
403 experiments, phase I, *US Bureau of Mines Report Investigation 7596*.

404 Vernik, L., and C. Landis (1996), Elastic anisotropy of source rocks: Implications for
405 hydrocarbon generation and primary migration, *AAPG Bull.*, 80, 531-544.

406 Viggiani, G. (2009), Mechanisms of localized deformation in geomaterials: an experimental
407 insight using full-field measurement techniques, *Mechanics of Natural Solids*, 105-125.

408

409 **Appendix A**

410 We provide a code in MATLAB that reproduces the results of Figures 3C and 4B. Note that the

411 MATLAB Image Processing Library is required to run this code.

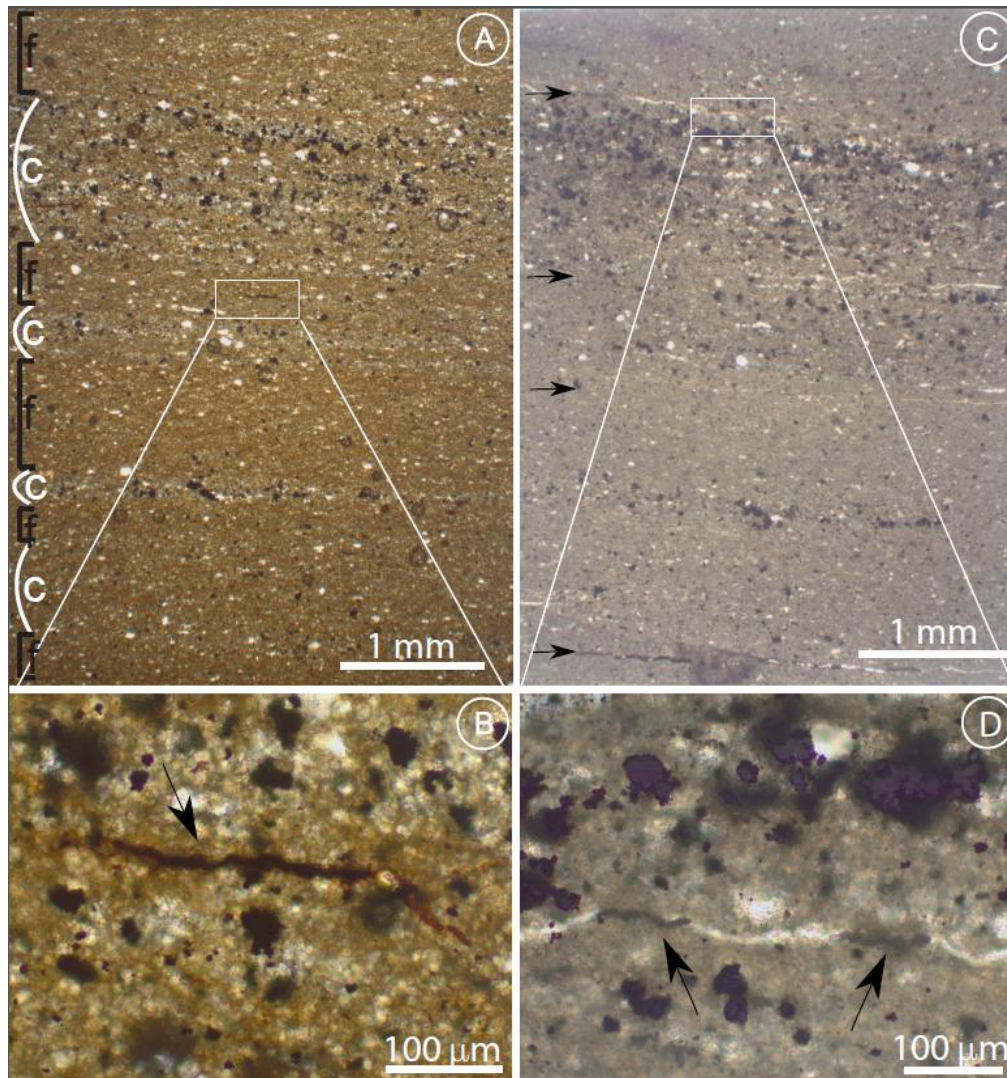
412

```
413 % Fiber bundle 2D model with local stress redistribution
414 L = 100; % The layer of shale has a size of LxL sites
415 sigmac = rand(L,L); % Random strength thresholds assigned for every site
416 fractured = zeros(L,L); % =1 if the site is fractured
417 dsigma = 0.15; % Amount of stress redistribution among the
418 unbroken neighbors when the site fractures
419 dp = 0.001; % Increment in pressure
420 pmax = 0.4; % Maximum value of pressure
421 pvalue = (0:dp:pmax); % Pressure range
422 nfrac = zeros(length(pvalue),1); % Number of fractured sites
423 nlargest = zeros(length(pvalue),1); % Size of the largest fracture
424 figure(1)
425 for ii = 1:length(pvalue)
426 % at each step of the program, pressure rises by the amount dp
427 p = pvalue(ii);
428 ndo = 1;
429 while ndo>0
430 ndo = 0;
431 i = find(sigmac<p);
432 % find the site with a breaking threshold lower than the pressure value
433 [ix,iy] = ind2sub(size(fractured),i); % find coordinates of this site
434 for j = 1:length(i)
435 if (fractured(i(j)) == 0)
436 fractured(i(j)) = 1;
437 % change the state of this site to fractured
438 nx = ix(j);
439 ny = iy(j);
440 xneighbors = [nx-1, nx+1, nx, nx]; % select the four
441 neighbors and find the edges of the system
442 yneighbors = [ny, ny, ny-1, ny+1];
443 k = find((xneighbors < 1) | (xneighbors > L) | (yneighbors <
444 1) | (yneighbors > L));
445 xneighbors(k)=[];
446 yneighbors(k)=[];
447 fracturedneighb = ones(1,length(xneighbors));
448 for m=1:length(xneighbors) % find neighbors which are broken
449 if fractured(xneighbors,yneighbors)==1
450 fracturedneighb(m)=0;
451 end
452 end
453 k=find(fracturedneighb == 0);
454 % remove neighbors which are broken
455 xneighbors(k)=[];
456 yneighbors(k)=[];
457 % distribution of stress among the non-broken neighbors
458 if (length(xneighbors) >= 1)
459 dsigmaN = dsigma*4/length(xneighbors);
```

```

460         for m=1:length(xneighbors)
461 % decrease the strength of non-broken neighbors
462             sigmac(xneighbors(m),yneighbors(m)) =
463 sigmac(xneighbors(m),yneighbors(m)) - dsigmaN;
464         end
465     end
466     ndo = ndo + 1;
467 end
468 end
469 end
470 nfrac(ii) = length(find(fractured>0)); % amount of fractured sites
471 [lw,num] = bwlabel(fractured); % assign a color to every fracture
472 img = label2rgb(lw,'jet','k','shuffle'); % label the fractures
473 s = regionprops(lw,'Area'); % measure the fracture area
474 area = cat(1,s.Area);
475 nlargest(ii) = max([max(area),0]);% find the area of the largest fracture
476 subplot(1,2,1)
477 imagesc(img); % plot the image of fractures
478 axis equal
479 axis tight
480 title('Fractures')
481 drawnow;
482 subplot(1,2,2)
483 plot(pvalue(1:ii)/pmax*100,nlargest(1:ii)/L^2*100,'r','linewidth',2);
484 %area of the largest fracture vs pressure
485 xlabel('Pressure,%')
486 ylabel('Fracture surface area,%');
487 axis([0 100 0 100])
488 axis square
489 drawnow
490 end
491

```



492

493 **Figure 1:** Thin section images of Green River Shale sample before and after heating. (A)

494 Interlaminated silt and clay-rich layers before heating. (f) clay-rich layers with higher amount of

495 kerogen lenses, (c) coarser layers with siliciclastic grains. (B) Detail of a kerogen lens. (C) Image

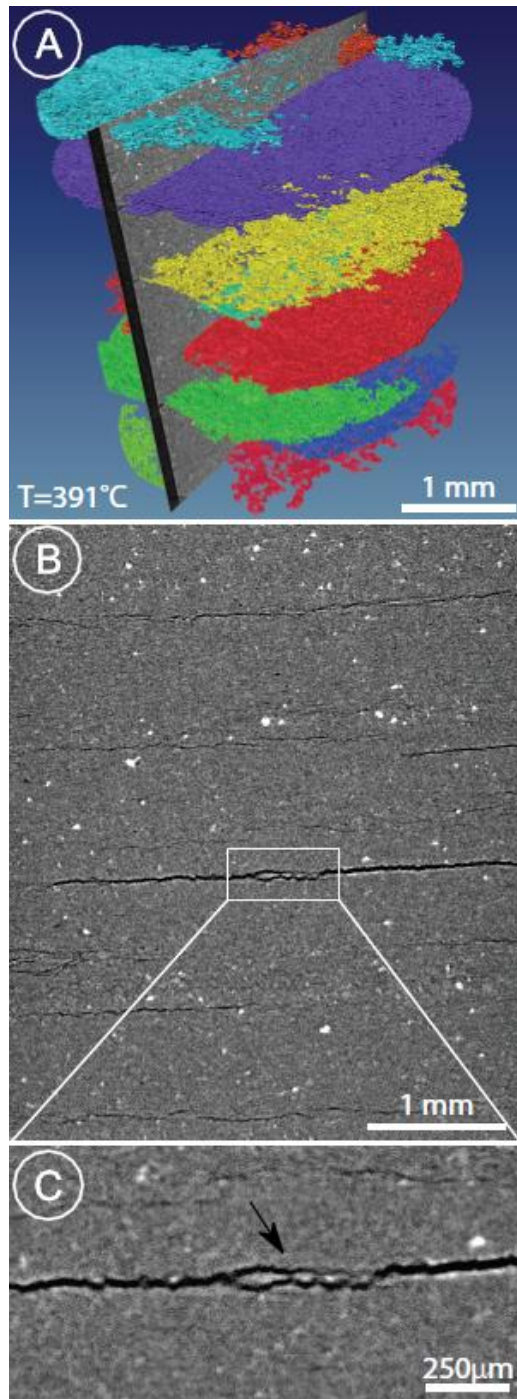
496 of the same sample after heating. Arrows indicate the position of cracks developed during

497 heating. Fractures propagated mainly in the finer grained intervals where the highest

498 concentration of organic matter lenses was also observed. (D) Detail of a crack filled with

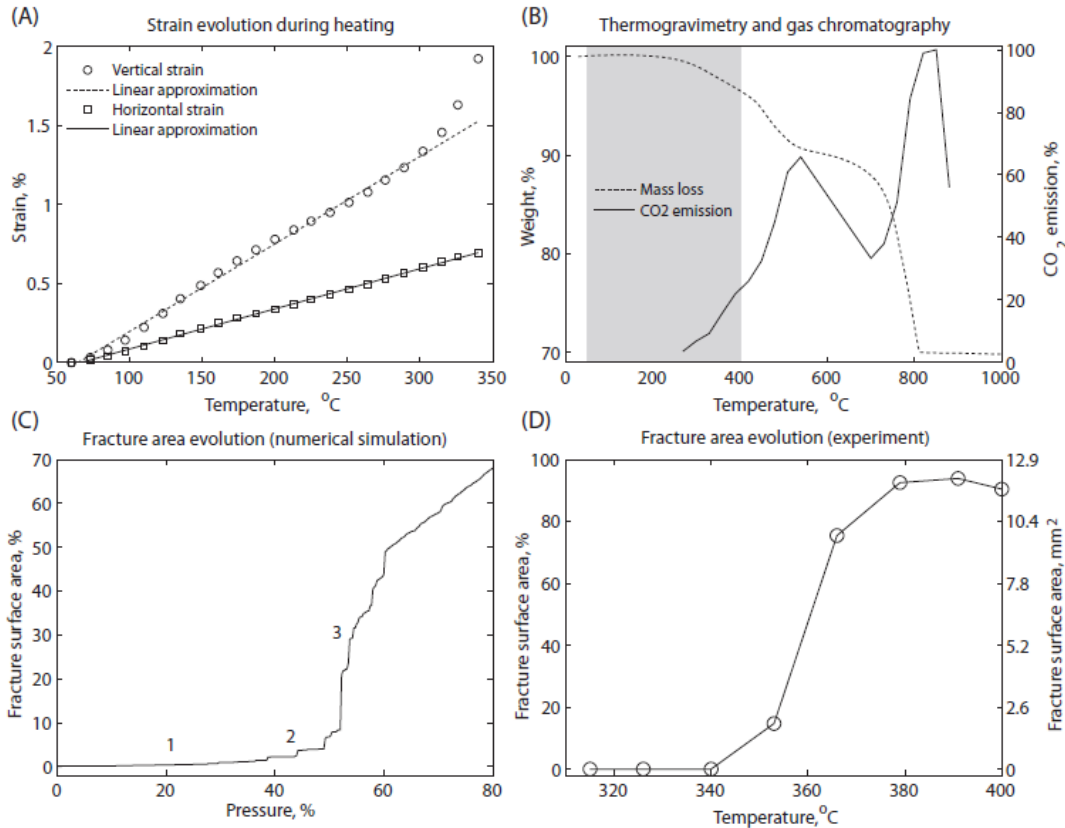
499 organic remains (arrows).

500



501

502 **Figure 2:** Tomography images of the shale sample at 391°C, corresponding to the moment of
503 maximum crack opening. (A) 3D rendering of final crack network. Each color defines an
504 independent crack. (B) 2D slice showing (dark color) elongated cracks developed parallel to the
505 bedding. (C) Detail of image (B) showing a crack developed around a pyrite grain (arrow).



506

507 **Figure 3:** Vertical and horizontal strain in a shale sample during heating. The linear relationship

508 between 70°C and 300°C corresponds to dilation of the sample due to thermal expansion.

509 Because of the anisotropy of the shale, the vertical and horizontal dilations are different. The

510 vertical strain-temperature relationship deviates from linearity at 300°C, at the onset of

511 degassing. Failure of the correlation technique at 350°C corresponds to the fracturing of the

512 sample. (B) Thermogravimetry (mass loss) and carbon dioxide emission analyses in aerobic

513 conditions. The change of slope on the mass loss curve at around 300°C occurs at the same

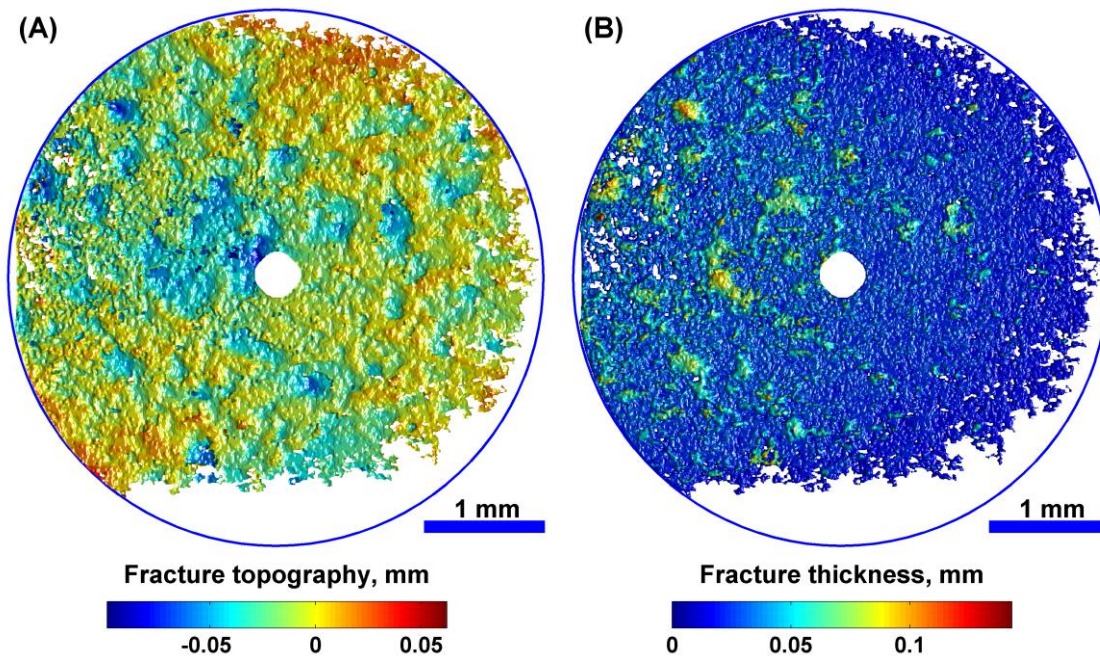
514 temperature as the onset of CO₂ production and corresponds to the onset of kerogen

515 decomposition. The grey shaded area indicates the temperature range of the tomography

516 experiment. The peak of CO₂ production and mass loss at around 800°C corresponds to the

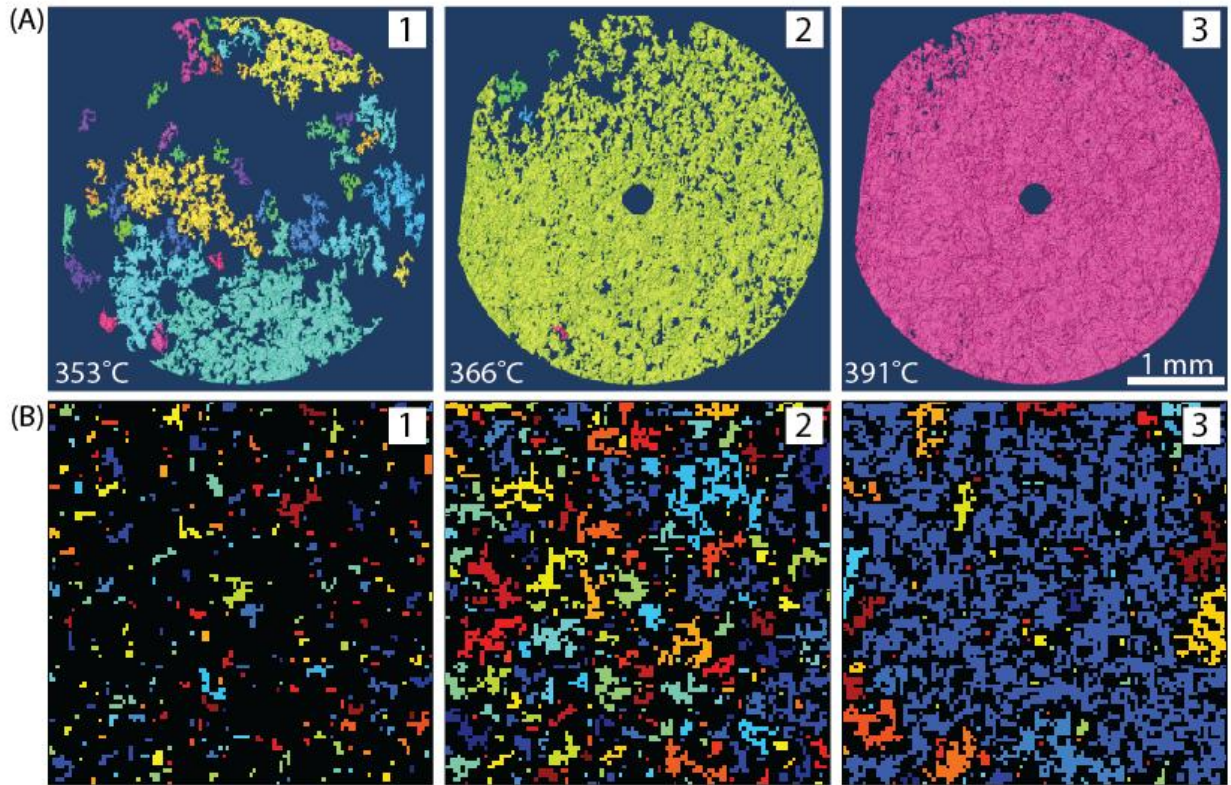
517 decomposition of carbonate. (C) Growth of the area of the biggest crack as a function of pressure

518 (% of maximum applied pressure) in the 2D lattice model. (1-3) – three stages of crack evolution
 519 corresponding to nucleation, growth and coalescence (see corresponding snapshots 1-3B in
 520 Figure 5). (D) Fracture evolution in the experiment. Growth of the surface area of the largest
 521 crack (in % of the sample cross-sectional area and in mm²) as a function of temperature. The
 522 slight decrease of fracture surface area observed after 390°C is attributed to partial crack closing
 523 after fluid expulsion.
 524

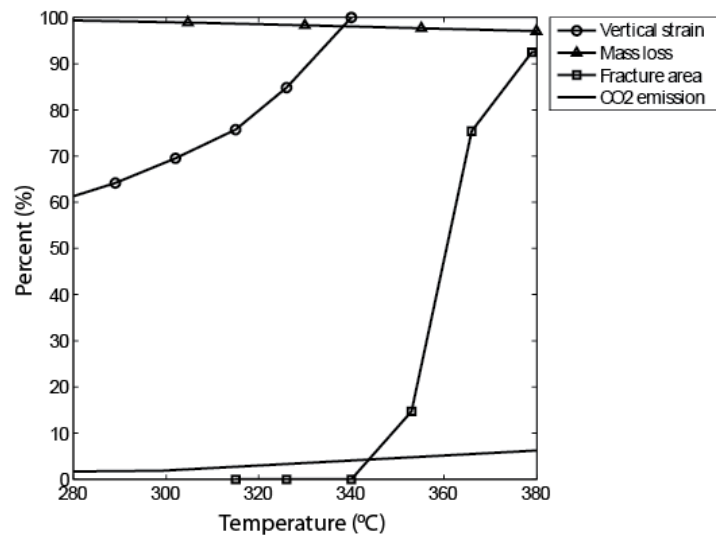


525
 526
 527 **Figure 4:** Reconstruction of the topography (top) and thickness (bottom) of a fracture extracted
 528 from Figure 2A. The circular central region in each image was removed because of a data
 529 acquisition artifact. The outer circle defines the boundaries of the sample. (A) Fluctuation of
 530 fracture surface height $h_1(x,y)$ around the fracture plane (x,y) is indicated by the color scale. The
 531 fracture front is irregular. The topography is created by small heterogeneities (i.e. pyrite
 532 minerals) that pin the fracture during its propagation. (B) The fracture thickness, taken as the

533 difference between the upper surface $h_1(x,y)$ and lower surface $h_2(x,y)$ of the fracture, is
534 indicated by the color scale. The thickness is quasi-constant and it is perturbed by pyrite
535 inclusions.
536



537
538 **Figure 5:** Comparison of crack evolution in the experiment and numerical model. (A) Crack
539 propagation dynamics during heating in the experiment. View of the cracks in a kerogen rich
540 layer viewed from a direction perpendicular to the average plane of the cracks. (1) Numerous
541 small cracks nucleated at $\sim 350^\circ\text{C}$. Each crack is indicated by a different color. (2) Cracks grew
542 and merged with increasing temperature. (3) Ultimately all cracks merged into a single sample-
543 wide crack. The circular central region in each image was removed because of a data acquisition
544 artifact. (B) 2D lattice model at three stages of crack development: nucleation (1), growth (2) and
545 coalescence (3) of cracks (see three stages of the area growth (1-3) in Figure 3C).



546

547 **Figure 6:** The correlation between vertical strain evolution (perpendicular to the shale
 548 lamination) during heating, mass loss, CO₂ emission and growth of fracture area in the shale
 549 sample. The onset of the mass loss and CO₂ emission corresponds to decomposition of organic
 550 material. The nonlinear strain growth in the vertical direction, which is caused by internal fluid
 551 pressure buildup, leads to the fracturing at 340°C.

552

(A)

0,84	0,69	0,76	0,79	0,85
0,79		0,78 -0,15	0,63	0,97
0,87	0,72 -0,15	 0,6	0,71 -0,15	0,68
0,68	0,89	0,75 -0,15	0,82	0,61
0,81	0,84	0,92	0,71	0,88



553

554 **Figure 7:** Sketch of the 2D discrete model. (A) The rock layer is modeled by a lattice of sites
 555 with assigned breaking thresholds. When a site fractures the stress is distributed equally to the
 556 non-broken neighbors, making them weaker. Two fractured neighbors are called a continuous
 557 crack. (B) The cracks grow by including new neighboring broken sites. When two cracks
 558 coalesce they form a bigger crack.